SNS Superconducting Linac Beam Dynamics

Dong-o Jeon

SNS Building MS-8218, Oak Ridge National Laboratory
104 Union Valley Road, Oak Ridge, TN 37831-8218, U.S.A.

SNS/ORNL/AP TECHNICAL NOTE

Number 012

This is a part of the report on the superconducting option of the SNS linac.

2.3 Beam Dynamics

2.3.1 Interfaces and Configuration

The beam matching and particle tracking for the SC SNS linac were carried out using the configuration described in Table 2.3. The normal conducting section was taken from the present SNS design up to 194.3 MeV, and the parameters shown in the table pertain to the CCL at that energy. The quadrupole average field widths were taken to be 8 cm in the CCL and 40 cm in the superconducting sections. The spaces between the doublet pairs in the SC linac were taken to be 30 cm. The doublet lattice periodicity was 5.839 m in the b_g=0.61 superconducting section and 7.700 m in the b_g=0.76 superconducting section.

Table 2.3 Linac configuration used in matching and tracking calculations

Linac Type	Normal Conducting Linac (CCL)	Superconducting b_g=0.61	Superconducting b_g=0.76
Energy Range (MeV)	79.2 -> 194.3	194.3 -> 336.8	336.8 -> 1000
Lattice Type	FODO	Doublet	Doublet
Lattice Period (m)	2.451 (at 194.3 MeV)	5.839	7.700
B' (T/m)	17.40	5.15	5.15
Energy Gain / Cavity (MeV)	2.4	4.71~5.55	6.45~8.93
RF Phase	–30°	–21°~ –33°	–26.5°

2.3.2 Matching

Beam matching was carried out using the code TRACE 3D [2.4] under the assumption of full beam current of 56 mA, a cavity frequency of 805 MHz, and 4.4×10^8 H^- ions per micorpulse. The TRACE 3D code transports a beam ellipse in 6D phase space linearly through a user-defined lattice. Space charge forces are treated linearly using a constant density model and the parameters of the beam ellipse. The initial step in the matching was the calculation of periodic solutions, within FODO or doublet lattice periods, for a number of periods on either side of the warm CCL to cold linac b_g =0.61 transition. The CCL parameters were taken as given, and the doublet quadrupole field gradient B' and the RF phase were adjusted in the b_g =0.61 section to give continuous phase advances per unit length for both transverse and longitudinal motion across the transition. The results, listed in Table 2.3, were $B' = 5.15$ and f=–21°. A similar procedure was carried out for the transition from the b_g =0.61 section to the b_g =0.76 section. In this case the doublet quadrupole field gradient of $B' = 5.15$ in the b_g =0.61 section and the RF phase of f=–26.5° in the b_g =0.76 section were taken as given, and the quadrupole field gradient in the

b_g =0.76 section and the RF phase in the b_g =0.61 section were varied. The results in this case were $B' = 5.15$ in the b_g =0.76 section and f=–33° in the b_g =0.61 section. In order to accommodate the different phases required at the low energy and high energy ends of the b_g =0.61 section, the RF phase was ramped linearly from f=–21° to f=–33° by 1.5° through each of the 9 cryostats in the b_g =0.61 section. The continuity in phase advance per unit length obtained by this procedure is for the periodic solutions.

Table 2.4 Parameters for matching between the CCL and the b_g =0.61 section.

Parameter Varied	Value
CCL Quadrupole Gradient	-14.85 T/m
CCL Quadrupole Gradient	11.59 T/m
1st Quad of SC Doublet	-5.008 T/m
2nd Quad of SC Doublet	4.804 T/m
1st SC Cavity RF Phase	-9.36°
4th SC Cavity RF Phase	1.10°

After completion of this preliminary matching to provide continuity in the transverse and longitudinal phase advances of the periodic solutions, the Courant-Snyder parameters of the 6D phase space beam envelope for these solutions are matched across each transition. Six lattice parameters were varied in each transition region to facilitate the match. Because there are four transverse dimensions and two longitudinal dimensions in the 6D phase space, it is natural to select four quadrupole field gradients and two RF cavity phases to vary. To carry out the match from the warm CCL into the b_g =0.61 section of the SC linac, the final two quadrupoles in the CCL, and the first doublet pair and the first and the fourth cavities in the SC linac were selected for variation of field gradients and RF phases, respectively. The resulting parameters, listed in Table 2.4, are easily attained and provide a precise match of the periodic solution in the CCL to that in the b_g =0.61 section.

The match between the b_g =0.61and b_g =0.76 sections was not necessary. Both TRACE3D and multiparticle simulations show that matching is already good enough.

Figure 2.4 is a TRACE 3D plot summarizing the beam transport for a matched solution from the 79.2 MeV low energy end of the CCL through the CCL, the b_g =0.61 section, and into the b_g =0.76 section. Thus, beam is transported through both matching sections. The upper figures show the initial (left) and final (right) beam ellipses in transverse (upper) and longitudinal (lower) phase space. The plot at the bottom shows the horizontal (top), vertical (bottom), and longitudinal (heavy curve at top) amplitudes through the transport. The transition from FODO to doublet solution is seen at the CCL to b_g =0.61 matching section, and a less dramatic transition is observed at the b_g =0.61 to b_g =0.76 match. In the superconducting linac, the envelope size never exceeds 1 cm in

the transverse direction or 5° in the longitudinal direction, indicating that the matched beam is well-behaved.

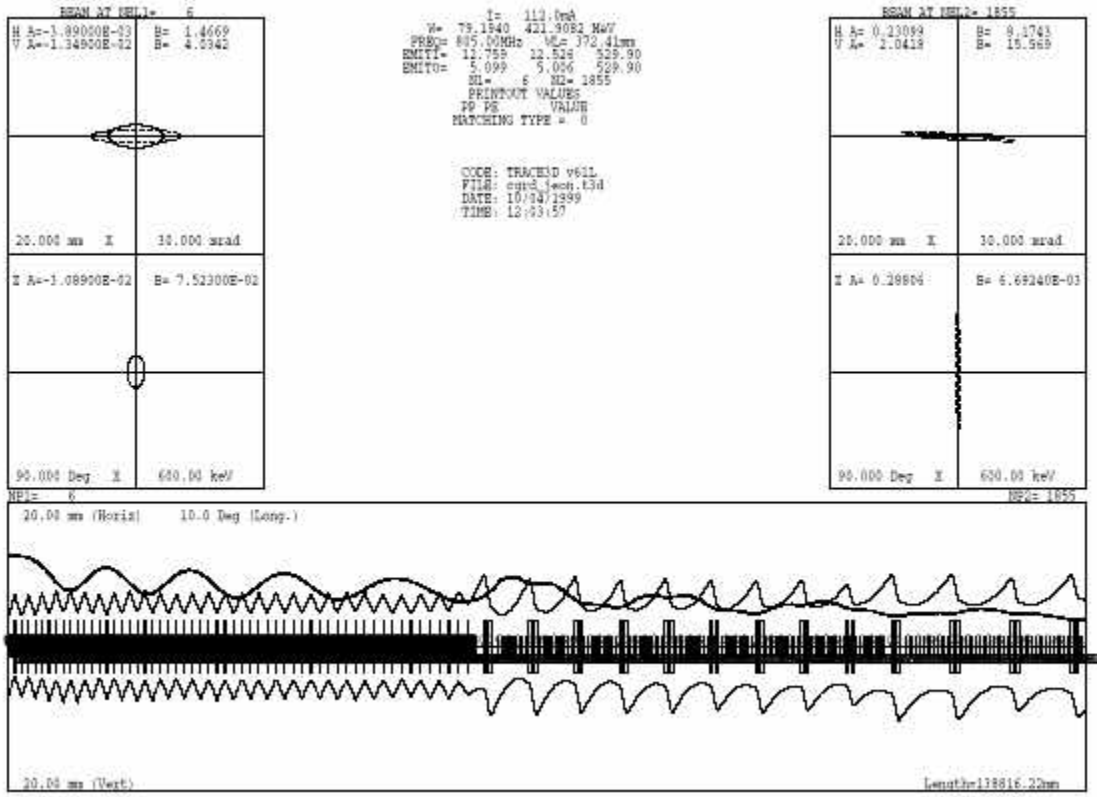

Fig. 2.4 TRACE 3D beam transport through the matching sections.

2.3.3 Multiparticle Simulations without Errors

In order to verify the overall architecture and matching, a more detailed beam dynamics calculation was carried out using multiparticle simulations. First without errors in the linac, using the LINAC Code and the old version of the PARMILA Code [2.5] and the lattice obtained from the previous TRACE 3D matching. The PARMILA Code was used for the simulations in the MEBT and DTL, while the LINAC Code was used in the CCDTL, CCL and the SC linac. Both codes carry out particle tracking treating the space charge interaction nonlinearly via a two dimensional PIC model in cylindrical geometry, with rotational symmetry about the beam axis. In the calculations a beam of 10,000 macroparticles was tracked from an initial distribution at the beginning of the RFQ to the end of the SC linac at 1.0 GeV. The initial distribution was taken from the tracking calculations including errors [2.6] starting with an initial 4D waterbag distribution at the entrance to the RFQ. Figure 2.5 shows that, without errors, the rms emittances in the horizontal, vertical, and longitudinal directions remain below $0.4p$ mm-mrad throughout the linac. Figure 2.6 shows, for the same calculation, the values of the maximum and rms

particle transverse displacements, and shows that the maximum transverse displacements are less than 1.5 cm throughout the linac. Both figures show that the optical matching between the interfaces is satisfactory.

Although these calculations are a preliminary match describing the beam dynamics of a 6-cell cavity SC pulsed H^- linac, they indicated that the behavior of the beam is quite acceptable, clearing the 5-cm radius in the SC section with 3.5 cm to spare. Figures 2.7 and 2.8 show the beam distribution at the beginning and at the end of the SC linac respectively.

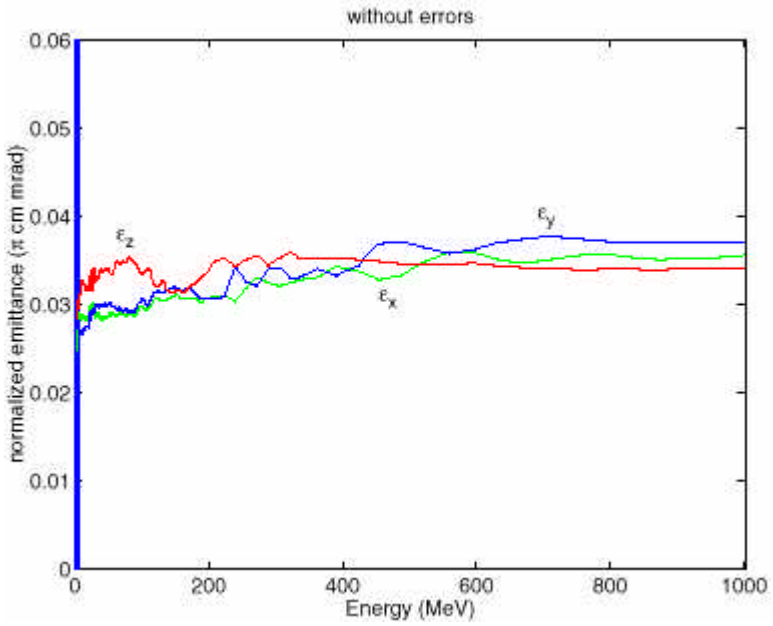

Fig. 2.5 LINAC calculation of the RMS beam emittances through the matched SC linac versus energy.

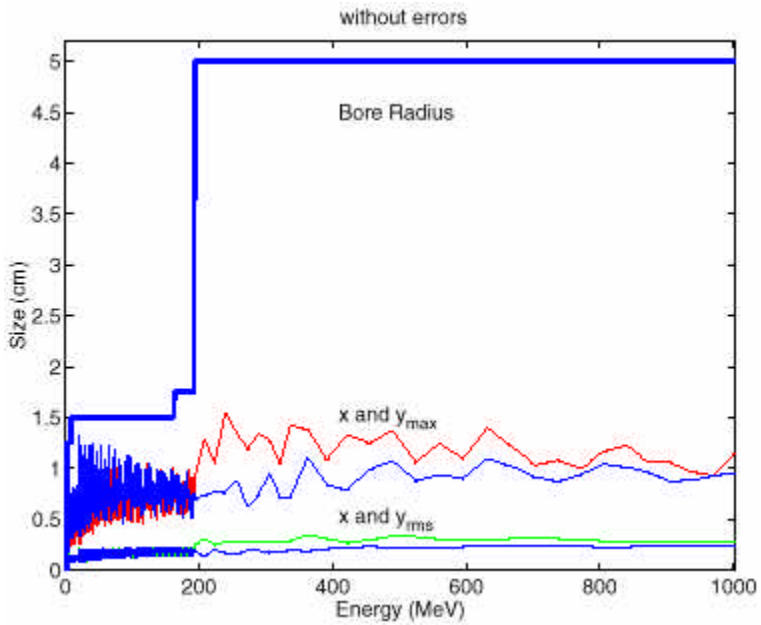

Fig. 2.6 LINAC calculation of the maximum and RMS transverse particle displacements through the matched SC linac

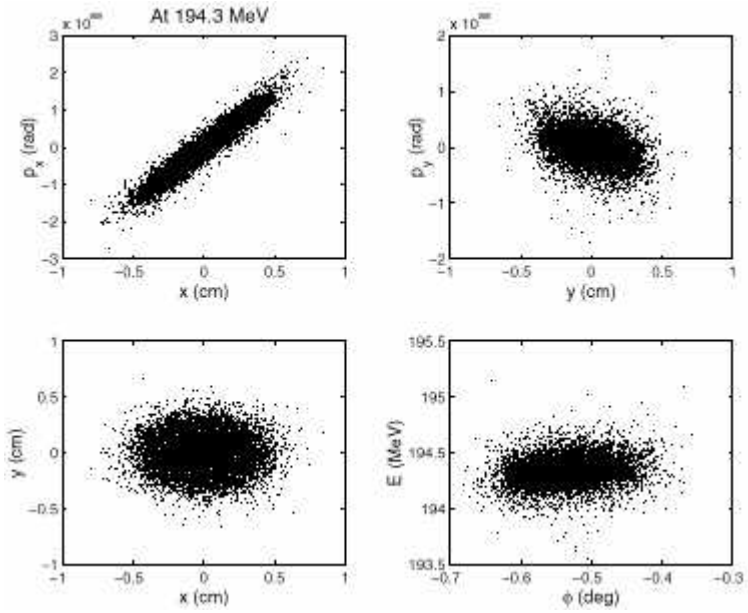

Fig. 2.7 Beam distributions at the beginning of the SC linac at the design energy of 194.3 MeV.

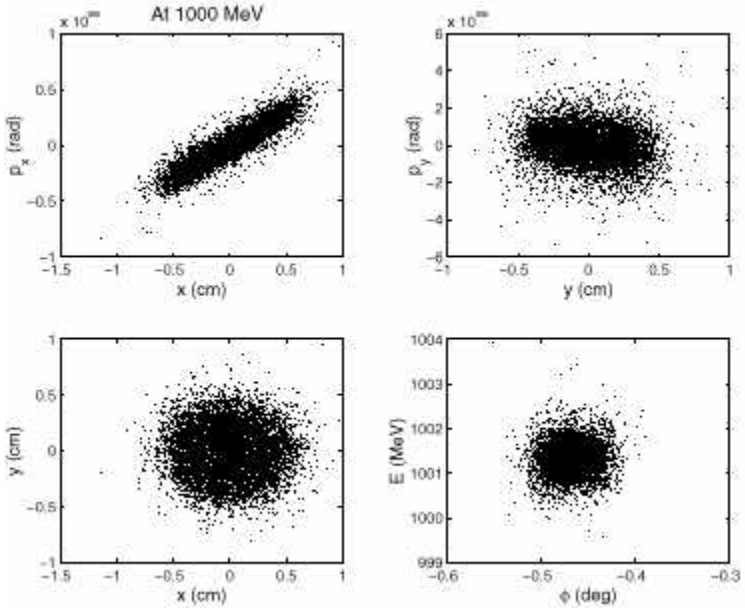

Figure 2.8 Final beam distributions at the end of the SC linac.

2.3.4 Multiparticle Simulations With Errors

A preliminary study on the tolerances of possible errors in the normal conducting linac and the superconducting linac was carried out. Table 2.5 lists the values of error limits on the warm FRQ, MEBT, DTL, CCDTL, and CCL. And Table 2.6 lists the values of error limits on the two sections of the superconducting linac used in this study. Microphonics was not included in the superconducting linac errors because it has been demonstrated that it is not a concern. Figure 2.9 shows the plots of the energy centroid jitter and the phase centroid jitter with the above errors. These results were obtained from the 10000 independent linac calculations from the CCDTL at 20 MeV to the end of the SC linac at 1000 MeV. These histograms show that under these assumptions, the energy spread from the SC linac should be correctable with the existing HEBT RF cavities and be acceptable for ring injection.

Figure 2.10 shows the normalized rms emittances for ten calculations. Each calculation uses different random number seeds, thus simulating ten independent linacs with errors. The number of macroparticles used in the simulations is 10,000. The maximum transverse extent of the 10,000 macroparticles in the beam and the rms beam sizes are shown in Fig. 2.11. The maximum transverse extent of the beam radius is well below 2 cm.

Table 2.5 Values of error limits of the MEBT, DTL, CCDTL, and CCL.

	MEBT	DTL
Quadrupole transverse displacement	0.0508 mm (2 mil)	0.0508 mm (2 mil)
Quadrupole roll	4.36 mrad (0.25°)	4.36 mrad (0.25°)
Quadrupole tilt	9.95 mrad (0.57°)	9.95 mrad (0.57°)
Quadrupole gradient error	1.732 %	0.5 %
Rf field phase error in tank	8.73 mrad (0.5°)	8.73 mrad (0.5°)
Rf field amplitude error in tank	0.5 %	0.5 %
Rf field tilt error in tank	0.1 %	0.1 %

		CCDTL and CCL
Quadrupole transverse displacement	EQD	0.127 mm (5 mil)
Quadrupole roll	EQR	5.0 mrad
Quadrupole tilt	EQT	5.0 mrad
Quadrupole gradient error	EQS	0.25 %
Error in distance between end gaps of adjacent segments	EDBC	0.254 mm (5 mil)
Error in distance between adjacent gaps of a segment	ECAVL	0.0508 mm (2 mil)
Segment transverse displacement	ESD	0.25 mm at ends (a)
Module field amplitude error (dynamic)	EFM	0.5 %
Module phase error (dynamic)	EPHM	0.5°
Module field amplitude error (static)	EFSET	1.0 %
Module phase error (static)	EPSET	17.45 mrad (1°)
Segment field amplitude error (static)	EFS	1.0 %
Segment phase error (static)	EPHS	0.0
Field amplitude tilt in module	EFTILT	1.0 % at ends (b)

a) independent misalignments of the two ends, resulting in displacements and tilts
b) lows at one and high at the other, or vice versa

Table 2.6 Values of error limits of the two sections of superconducting linac.

		Low beta section	High beta section
Doublet transverse displacement	EDD	0.127 mm	0.127 mm
Doublet rotation	EDR	5.0 mrad	5.0 mrad
Doublet tilt	EDT	5.0 mrad	5.0 mrad
Doublet gradient error	EDS	0.25 %	0.25 %
Cavity displacement within cryostat	ECAVD	0.0508 mm	0.0508 mm
Klystron amplitude error	EKAD	0.5 %	0.5 %
Klystron phase error	EKPHD	0.5°	0.5°

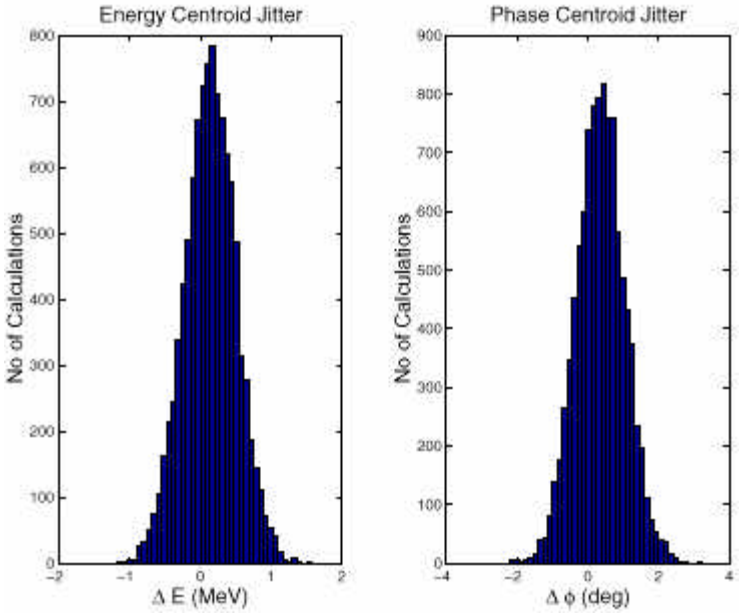

Fig. 2.9 Histogram of the energy centroid jitter and the phase centroid jitter due to errors for 10,000 linac runs.

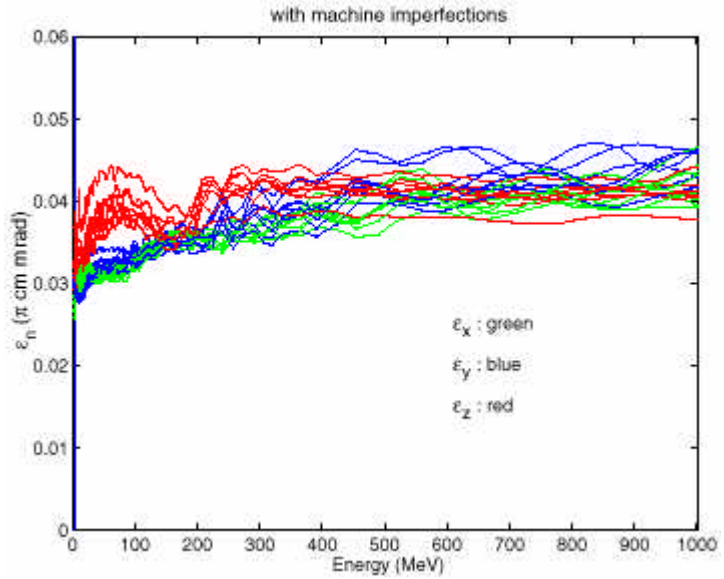

Fig. 2.10 Normalized rms emittances versus energy for 10 independent runs with about 10,000 macroparticles. Each run was done with different random number seeds for simulating errors.

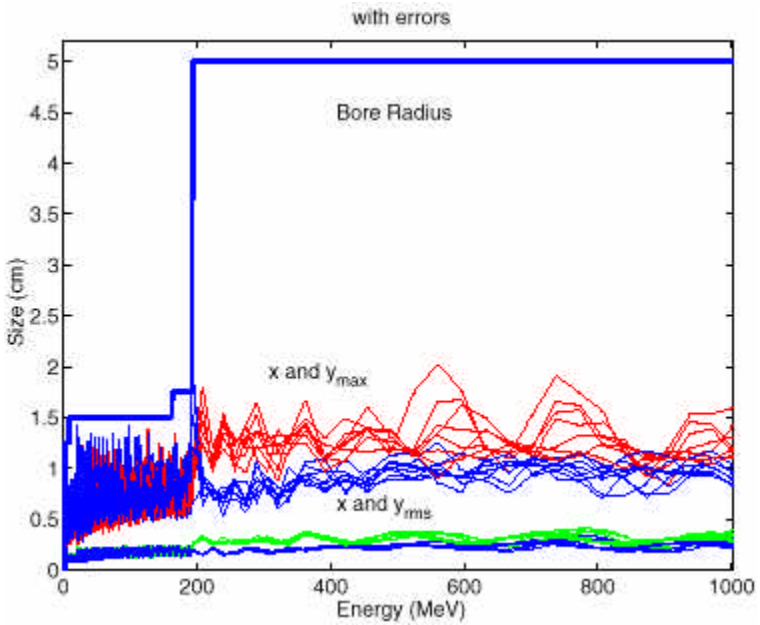

Fig. 2.11 The maximum transverse extent of the macroparticles in the beam and the rms beam sizes versus energy for 10 independent runs with about 10,000 macroparticles. Each run was done with different random number seeds for simulating errors.

2.4 Cavity failure simulations

The effects of cavity failure are simulated without any linac errors. A failure of two cavities in the same cryomodule of the high beta section turns out not to be critical to the linac operation as is shown in Fig. 2.12 where the transverse and longitudinal normalized rms emittances are plotted vs. energy. Figure 2.13 shows the transverse and longitudinal emittances when two cavities in the same cryomodule of the low beta section fail. In this case the emittance growth is more pronounced due to the stronger space charge effects. However, we can reduce either the transverse rms emittances or the longitudinal emittance depending on which of the two is more critical. This can be done by choosing a proper set of cavities and quadrupole doublet pairs for rematching. Figure 2.14 shows two different cases of rematching. When the transverse emittances are more critical, for example, we can choose the rematching scheme 1 where the transverse emittances are reduced at the price of increased longitudinal emittance. Nonetheless the linear sum of emittances can not be reduced at the same time. Figure 2.15 shows the beam distribution in phase spaces right after passing through the two failed cavities of the low beta section. Due to the cavity failure, a significant deformation in the longitudinal phase space takes place, which in turn induces strong envelope oscillations and halo formation. Through the coupling, a significant enhancement of halo formation in the transverse phase spaces is also induced. The resultant halo is well demonstrated in Figure 2.16. The total energy spread is ±1.2 MeV, whereas the total energy spread of the core is only ±0.5 MeV. On top of this energy spread in the bunch, the centroid energy total jitter is ±1.1 MeV (see Fig. 2.9), which is half of the requirement ±2.2 MeV. These conditions are quite acceptable considering the energy acceptance of the ring. Besides, in HEBT line there

are momentum collimators at ±3.0 MeV, which will intercept the halo particles with large energy spread.

Multiparticle simulations indicate that a complete failure of one cryomodule is not tolerable in both low beta and high beta sections. The total energy spread in the bunch is ±2.5 MeV and the longitudinal phase space is severely distorted (refer to Fig. 2.18). Considering the energy centroid total jitter of ±1.1 MeV on top of this energy spread in the bunch, the total energy spread is not tolerable to the ring energy acceptance. Figure 2.17 shows the normalized rms emittance growth due to the failure of one cryomodule in the high beta section. The growth of the transverse and the longitudinal emittances is appreciable.

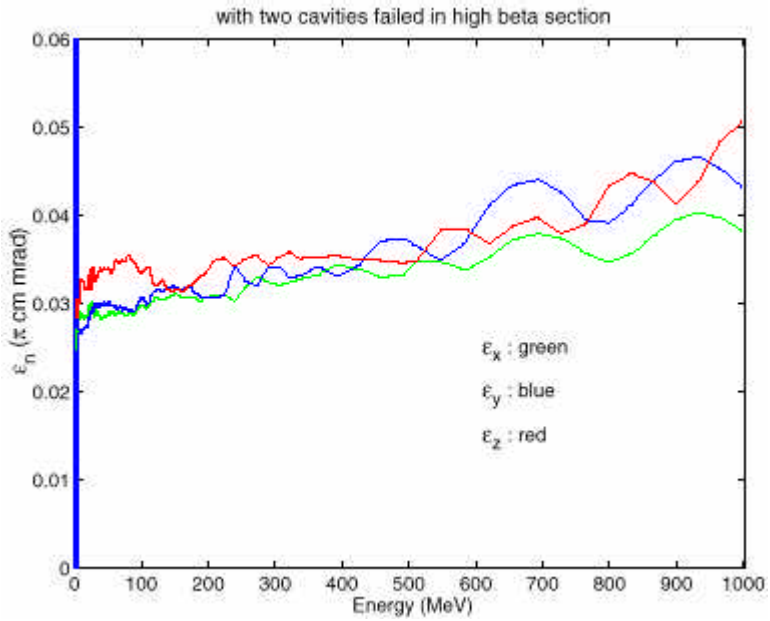

Fig. 2.12 Plots of normalized transverse and longitudinal emittances when two cavities in the high beta section fail at about 550 MeV.

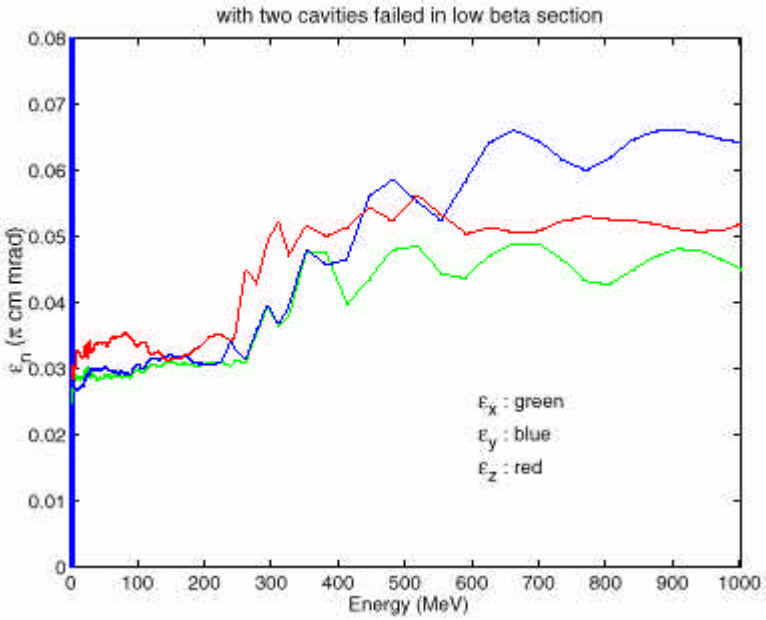

Fig. 2.13 Plots of normalized transverse and longitudinal emittances when two cavities in the low beta section fail at about 262 MeV.

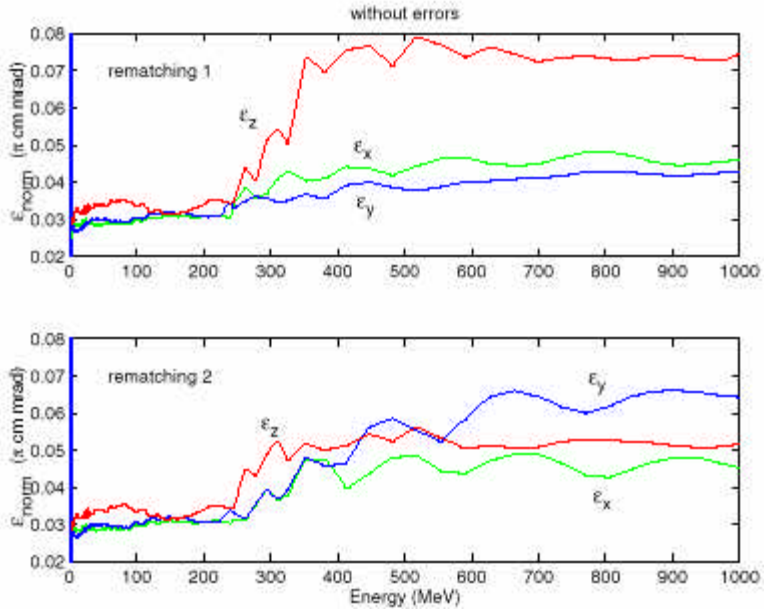

Fig. 2.14 Plots of normalized rms emittances for two different rematching by adjusting two cavities and four quadrupoles around the failed two cavities of the low beta section.

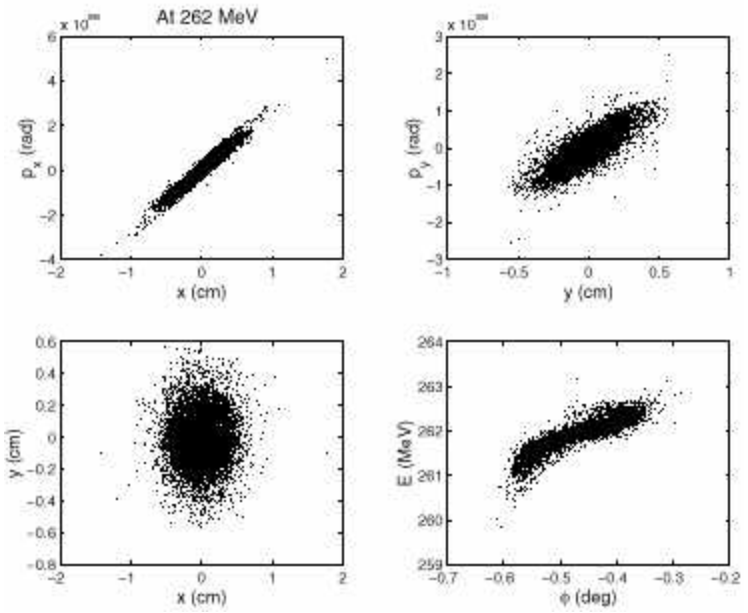

Fig. 2.15 Plots of beam distribution right after passing through the failed two cavities of the low beta section. A pronounced deformation in the longitudinal phase space is observed.

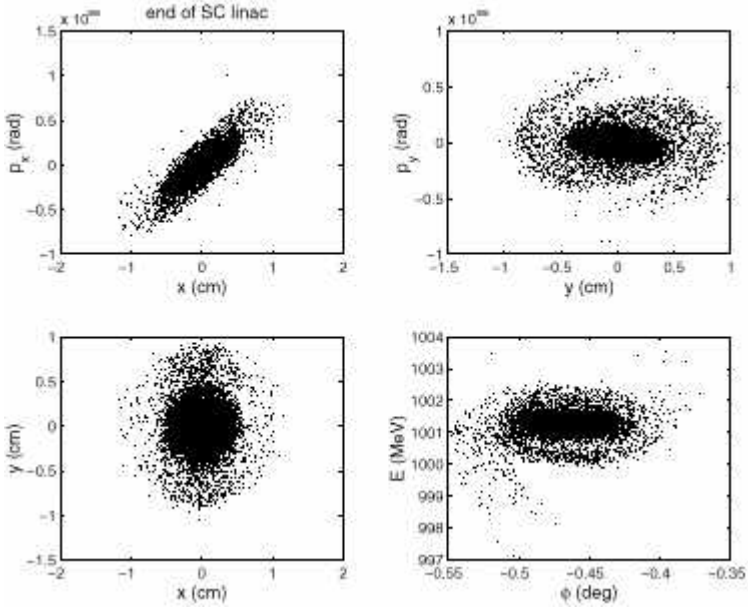

Fig. 2.16 Plots of distribution of the same beam in Fig. 2.15 at the end of the superconducting linac. Due to the coupling, halo formation takes place in the transverse phase spaces as well as in the longitudinal phase space, which leads to rms emittance growth.

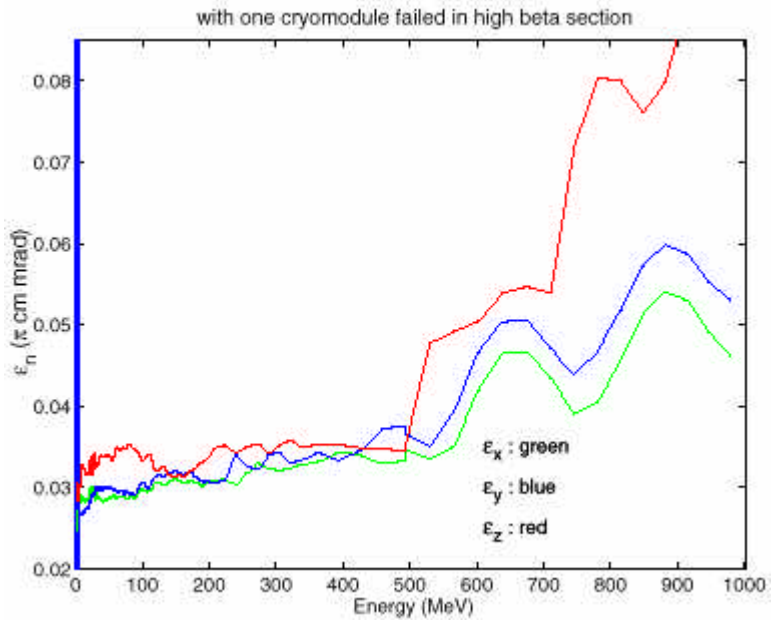

Fig. 2.17 Plots of normalized rms emittances when one cryomodule fails in the high beta section.

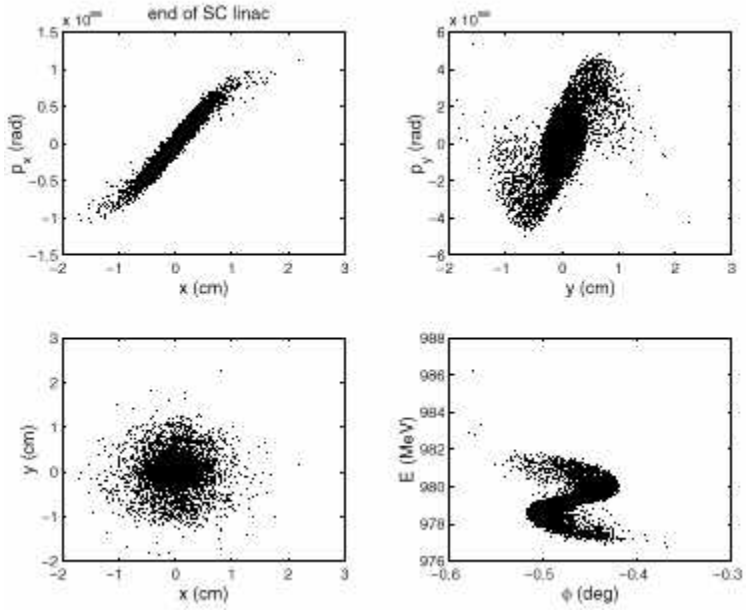

Fig. 2.18 Plots of beam distribution in phase spaces when one cryomodule fails in the high beta section before compensating the final beam energy. The energy spread of the bunch is ±2.5 MeV and a significant halo formation is induced.

2.5 Summary of Integrated Physics Design

A satisfactory SC linac architecture has been determined to accelerate the SNS H^- beam from 194.3 to 1001.5 MeV. This linac is 191.2 m long with 27 b_g =0.61 cavities, 9 cryomodules, and 80 b_g = 0.76 cavities, 20 cryomodules. The parameters of this linac are listed in Table 2.7.

A satisfactory 6D matching was obtained between the normal conducting linac and the b_g =0.61 section of the superconducting linac, and between the b_g =0.61 and the b_g =0.76 sections of the SC linac. Multiparticle simulations show that the emittance growth is minimal across the interfaces. Without errors, the normalized rms emittances grow from about 0.32 π mm-mrad at 194 MeV to about 0.35 π mm-mrad at 1 GeV. The maximum extent of the beam profile radius stays below 1.6 cm. The beam particle distributions at the final energy indicate that the halo formation is reasonable in all dimensions. Preliminary study on the effects of various errors was completed. The energy centroid jitter and the phase centroid jitter are both acceptable assuming 0.5% klystron amplitude errors and 0.5° phase errors in the SC linac with one RF system per cavity. More detailed systematic studies will be carried out.

APPENDIX Optimizer Studies

In order to understand the design choice for the optimum number of cells per cavity and also the quantitative difference between a constant-energy-gain per cavity and constant-gradient per cavity linac architecture, a simple computer code was written for the acceleration of the synchronous H- ion [2.1]. This code was used in a genetic optimizer shell to determine the optimum linac parameters under different assumptions. The ideal transit time factor for an individual cell was taken as Eq. 2.52 from Ref. 2.2 with end-cell correction factors to fit Superfish calculated transit time factors, average electric fields and cavity electrical centers. The resulting code was successfully benchmarked against existing SC linac synchronous particle calculations [2.3].

Two cavity sections with $\beta_g = 0.61$ and 0.76, were assumed for all cases. Six-cells per cavity and eight-cells per cavity were studied. The number of cavities per cryomodule are listed in Table 9. The lengths between cavities and cryostats were taken from Table 9.

The ratio of the peak surface electric field, E_{peak}, to the average gradient of an interior cell, $E_{0\text{-}int}$, and the peak surface magnetic field, B_{peak}, to $E_{0\text{-}int}$ were input for each cavity section and are also listed in Table 9. The peak surface electric field provides the fundamental limitation on the acceleration gradient and was limited to 27.5 MV/m, which corresponds to peak magnetic field of less than about 70 mT. KEK has built and tested input power couplers with peak power capabilities of 380 kW. For this study a conservative maximum coupler power of 350 kW was assumed. The average beam current for the 2 MW SNS beam during a macropulse is 36 mA. No other power losses are accounted for except beam power.

The problem formulation for the optimizer is listed below:

- The average phase per cavity for the first section was fixed and varied linearly from -21.0^0 to -33.0^0 and the phase of the second section phase was fixed at -26.5^0.
- The peak surface electric field was limited to be $\leq$ 27.5 MV/m.
- The power to each cavity or coupler was limited to be $\leq$ 350 kW.
- The number of cryomodules per cavity section was varied while minimizing the number of cryostats or total linac real estate length while accelerating the H- ions from 194.3 to 1001.5 MeV.
- The energy gain in each cavity section was held to a constant and varied allowing the cavity gradient to vary with transit time factor OR identical electric gradients in each cavity section were held constant and varied allowing the energy gain per cavity to vary with transit time factor.

Table 9 summarizes some parameters for the four optimized linac architectures. Some of the more important differences in these parameters are summarized below:

- The 6-cell linacs are shorter than the corresponding 8-cell linacs even though the filling factors are slightly smaller because (1) The 8-cell linacs tend to be limited by the coupler power limit, (2) The transit time factors for the 6-cell linacs are on average larger, (3) the phase spread over a cavity of a 6 cell linac is less, and (4) the

6-cell linacs are not limited by the end cavity gradients where the transit time factors are small.

- The difference between the 6-cell constant-energy-gain and constant-gradient linacs is essentially three cryostats or 16 meters of length. If the input RF power to each cavity can be varied, then the difference in these architectures would be an operational issue and a maximum gradient issue. With a constant-energy-gain architecture the cavities with the highest quench fields would be used at the end of the cavity sections where the highest gradients are required.

Table 9. Summary parameters for 805-MHz SC linacs from 194.3 to 1001.5 MeV.

Constant gradient or power	Gradient		Gradient		Power		Power	
Cells per cavity	6		8		8		8	
Total real estate length [m]	191.2		243.1		206.8		234.7	
Total cavity length [m]	79.5		108.3		84.3		102.0	
Energy gain per real estate m [MeV/m]	4.22		3.32		3.90		3.44	
Beta	0.61	0.76	0.61	0.76	0.61	0.76	0.61	0.76
Active cavity length [m]	0.681	0.849	0.908	1.132	0.681	0.849	0.908	1.132
$E_{peak}/E_{o\text{-}int}$	2.33	1.82	2.33	1.82	2.33	1.82	2.32	1.82
$B_{peak}/E_{o\text{-}int}$ [mT/MV/m]	4.64	3.86	4.64	3.86	4.64	3.86	4.64	3.86
B_{peak}/E_{peak} [mT/MV/m]	1.99	2.12	1.99	2.12	1.99	2.12	1.99	2.12
E_{peak} [MV/m]	32.6	29.1	32.6	21.7	32.2	32.4	30.4	318
B_{peak} [mT]	64.9	61.4	64.9	45.9	64.0	68.6	60.5	67.4
Max $<E_o>$[MV/m]	15.5	17.1	15.2	12.6	15.3	19.0	14.1	18.5
Min $<E_o>$ [MV/m]	15.5	17.1	15.2	12.6	12.1	16.0	9.95	12.9
Max energy gain / cavity [MeV]	6.39	9.58	8.54	9.50	5.05	8.98	5.61	9.68
Min energy gain / cavity [MeV]	5.28	7.21	6.08	6.48	5.05	8.98	5.61	9.68
Max peak power per cavity [kW]	230	345	307	342	182	323	202	348
Min peak power per cavity [kW]	190	260	219	233	182	323	202	348
No. cryomodules	9	18	11	26	13	17	15	22
No. cavities/cryomodule	3	4	2	3	3	4	2	3
No. cavities	27	72	22	78	39	68	30	66
No. of cells/cavity	6	6	8	8	6	6	8	8
Total section length [m]	52.5	138.6	56.1	187.0	75.9	130.9	76.5	158.2
Transition energy [MeV]	356.4	356.4	360.9	360.9	391.2	391.2	362.7	362.7
Fill factor	0.350	0.441	0.356	0.472	0.350	0.441	0.356	0.472
Average cavity TTF	0.688	0.698	0.665	0.663	0.684	0.707	0.670	0.661
Average cavity $<\cos f>$	0.798	0.824	0.752	0.757	0.787	0.832	0.759	0.768
Average cavity $<E_o>$	15.5	17.1	15.2	12.6	13.2	16.9	11.3	14.9

REFERENCES

2.1. ORNL SNS Accelerator Physics Internal Memo, Synchronous Particle Scoping Studies for an SNS SC Linac, 9/13/99, John Galambos, Jeff Holmes, Dong-o Jeon, and David Olsen.

2.2. T. Wangler, “Principles of RF Linear Accelerators”, J. Wiley & Sons, 1998.

2.3. T. Wangler, private communication, August 1999.

2.4 K. R. Crandall and D. P. Rusthoi, TRACE 3-D Documentation, Third Edition, LA-UR-90-4146, (Los Alamos National Laboratory, 1990).

2.5 B. Blind and R. Garnett, LINAC Code and old version of PARMILA Code, private communication, 1999.

2.6 J. Staples, private communication, 1999.